

Scientific Paper

Doi: <http://dx.doi.org/10.1590/1809-4430-Eng.Agric.v43n3e20230039/2023>

DISCRETE ELEMENT-BASED DESIGN OF KEY PARAMETERS FOR WHEEL RUT TILLAGE DEVICES

Haiyang Zhuang¹, Xianliang Wang^{1*}, Xiangcai Zhang¹,
Xiupei Cheng¹, Zhongcai Wei¹,

^{1*}Corresponding author. College of Agricultural Engineering and Food Science, Shandong University of Technology/Zibo, China.
E-mail: wx11990@sdtu.edu.cn | ORCID ID: <https://orcid.org/0000-0001-7099-6286>

KEYWORDS

discrete element method, soil lifting device, soil crushing device, soil disturbance, operating resistance.

ABSTRACT

In this study, a device was designed for tillage of compacted soil in wheel ruts formed by the repeated passage of agricultural machines. Soil parameters were measured, and then the wheel rut tillage device was divided into two parts, the soil lifting unit and the soil breaking unit, for separate simulation tests to study the tillage process. EDEM simulations were applied to the soil lifting device to compare and analyze the microscopic movement of the simulated soil particles and the operational resistance of the device. Analysis of variance (ANOVA) was performed using Design-Expert10 software to obtain the optimum combination of parameters of 125 mm device offset distance, 43.6° entry angle and 28° lifting angle. A full-factor test was conducted on the soil crushing device using EDEM coupled with RecuDyn multi-body system dynamics simulation software. The number of bond breaks and the traction resistance of the soil crushing device were used as the test indicators, and the optimum parameters were obtained for a soil crushing knife blade thickness of 6 mm and a cutting edge angle of 30° for the largest number of bond breaks and least traction resistance. The results of this study will provide technical support for the reduction of compaction zones in wheel ruts after tire travel on agricultural machinery in real time.

INTRODUCTION

With the accelerated mechanization of the entire process of production of all types of crops, mechanical compaction of the soil by the running gear of agricultural machinery has become a worldwide environmental problem that can significantly degrade the soil and lead to lower crop yields.(Chen & Weil, 2011; Berisso et al., 2012; Nawaz et al., 2012). Soil is a viscoelastic-plastic medium, and agricultural machinery travelling on soil deforms and compacts the soil. The repeated travel of machinery throughout the crop growth process transfers compacted soil from ruts made by wheels to other areas, resulting in severe and deep compaction of soil in the ruts.(Lamandé & Schjønning, 2011; Keller et al., 2014). Deep soil compaction is the main cause of inhibition of crops and is difficult to eliminate.(Ren et al., 2022).

Reducing the formation of compacted soil is the most effective way to prevent crop losses from compaction. The main ways of currently reducing the formation of soil

compaction are as follows: (1) Reducing the axle load and increasing the tire-soil contact area through the structural design of the tractor, increasing the tire-soil contact area and reducing the soil surface pressure can alleviate soil compaction to some extent. Changing the tractor structure from two-wheel drive to four-wheel drive can equalize the compaction effects of the front and rear wheels on the soil (Hamza & Anderson, 2005). (2) Using no-till as an alternative to conventional tillage reduces the process of cumulative compaction of soil by reducing the number of applications of farm machinery. In addition, mulching crop residues on the surface reduces surface soil compaction (Gao et al., 2007; Sun et al., 2023). (3) Using fixed channel systems reduce the impact of soil compaction on crop growth (Chen & Yang, 2012).

Mechanized tillage technology is an effective way to quickly reduce soil compaction and improve the structure of the tillage layer (Gao et al., 2020). Mechanized tillage technology improves the environment for crop growth mainly by changing the trophic relationship of the soil, but it cannot

¹ School of Agricultural Engineering and Food Science, Shandong University of Technology/Zibo, China.

Area Editor: Fábio Lúcio Santos

Received in: 3-12-2023

Accepted in: 9-11-2023

repair the structural breaks in the soil caused by compaction. There are still problems with the current application of mechanized tillage, such as the short duration of the loosening effect, secondary compaction and high operating resistance. The negative effects of compaction on soil are a cumulative process, and once compaction has occurred, it is more difficult to repair. Progress has been made by using equipment that follows farm machinery to plow compacted soil and prevent damage to the soil from cumulative compaction (Schjønning et al., 2013).

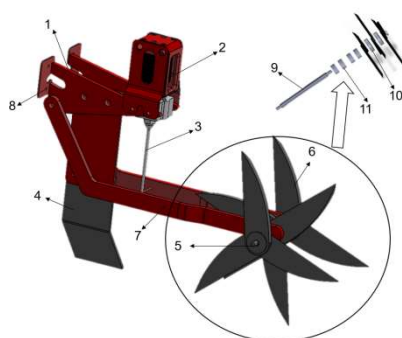
In this study, we design a wheel rut tillage device with the aim of reducing the operating resistance, breaking the bonds and lifting the soil to prevent cumulative soil compaction in wheel ruts caused by agricultural machinery. At the same time, we combine discrete element simulation and RecuDyn multi-body system dynamics simulation in research to analyze the forces on the wheel rut tillage device during the soil working process to provide a theoretical basis and technical

support for researching the problem of cumulative compaction of soil in wheel ruts that cannot be eliminated.

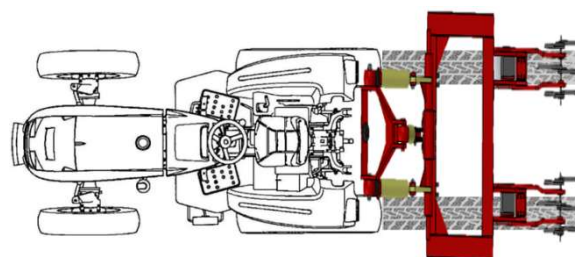
MATERIAL AND METHODS

Overall Structure

The designed pair of wheel rut tillers mainly consists of triangular connecting plate 1, spring-down device 2, spring-down connecting rod 3, soil lifting device 4, shaft 5, soil crushing knife 6, soil crushing knife fixing bracket 7, and bolt hole 8. The overall structure is shown in Figure 1(a). The soil lifting device is located at the front of the soil crushing blade, and its basic function is to lift the soil after the tire is pressed, as shown in Figure 1(b). As the soil lifting device moves forward, the inner side pushes the soil particles upward so that the soil compacted by the tires is lifted and broken more effectively by the soil breaking blade at the rear end to loosen the soil.



(a) Overall structure of the wheel rut tillage device



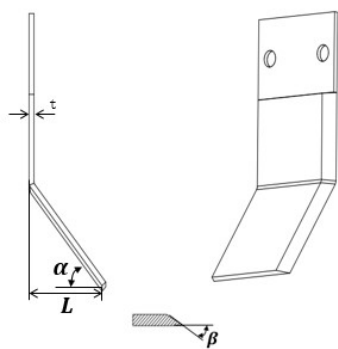
(b) Operation of the device

FIGURE 1. 1. triangular connecting plate, 2. spring down device, 3. spring down connecting rod, 4. soil lifting device, 5. Shaft, 6. soil crushing knife, 7. soil crushing knife fixing frame, 8. bolt hole, 9. hexagonal shaft, 10. Bearing, and 11. Sleeve.

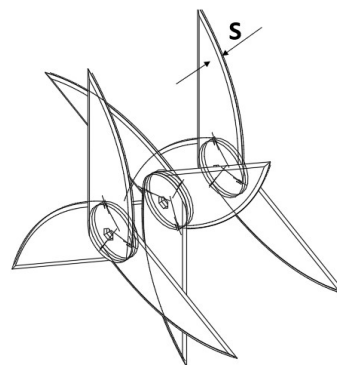
Working Principle

When working in wheel ruts, the soil lifting device should be placed perpendicular to the ground. When acting on the wheel rut, the soil lifting device and the soil crumbling device work together, and the soil lifting device exerts a forward and upward force on the soil in the wheel rut. The offset distance L of the soil lifting device, the soil entry angle α , and the lifting angle β of the soil lifting device have obvious effects on the displacement of soil particles, while the soil

crushing device produces a normal chopping force and a tangential slip-cutting force on the soil. The blade thickness S and blade angle of the soil crusher have a significant effect on the slip-cutting force. The direction of the slip-cutting force is backward and downward, which is opposite to the direction of the soil force of the soil lifting device, which can increase the slip-cutting effect and reduce the cutting resistance. When acting on the soil, the soil is broken by the operation of the soil lifting device and the soil crushing device, and the soil is loosened.



(a)



(b)

FIGURE 2. (a) Details of the entry angle, lifting angle and offset distance of the soil lifting device, (b) thickness of the soil crushing knife

Force analysis of particles under the action of the shovel tip of the soil lifting device

The tip of the bucket causes shear failure on the face of the soil, and the bonded soil breaks and lifts under the action of the bucket wall. The force analysis of the tip of the soil lifting device can be found in Soehne et al. (Gill et al., 1983) for the analysis of the inclined working part as it makes a linear motion in the soil. The tip is subjected to the traction force of the traction machine, the friction and cutting

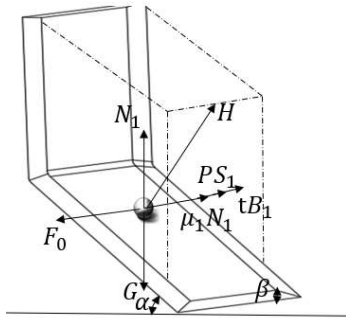


FIGURE 3. Analysis of the force on the shovel tip.

The tip of the bucket and the bucket handle are mainly subjected to the adhesion resistance, shear force, cutting force and frictional resistance of the soil, as shown in Figures 2 and 3. The combined force in the horizontal direction of the resistance to the tip of the bucket and the bucket handle is equal in magnitude and opposite in direction to F_0 , and F_3 so that:

$$F_0 = PS_1 \cos \alpha + \mu_1 N_1 \cos \alpha + tB_1 + N_1 \sin \alpha \quad (1)$$

$$F_3 = \mu_1 N_2 \sin \beta + 2\mu_1 N_3 \quad (2)$$

in which:

F_0 - the traction force on the tip of the earth lifting device,

F_3 - the traction force on the shank of the soil lifting device.

When cutting soil, shear failure begins to occur on the face of the soil block above the tip of the bucket. The soil above the tip of the bucket is subject to gravity, acceleration,

resistance between the soil lifting device and the soil, and the pressure of the soil on the soil lifting device. The main forces are subjected to a force analysis, and the schematic diagram is shown in Figure 3. When the soil lifting device operates, the soil in the deep layer moves forward under the action of the bucket handle, and the soil in the surface layer moves both forward and upward under the action of the bucket handle. By studying the soil cutting force, the force analysis diagram of the bucket handle is shown in Figure 4.

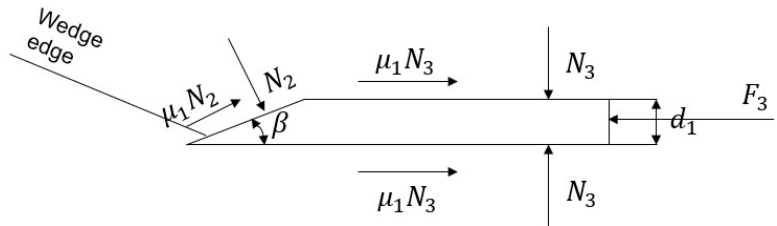
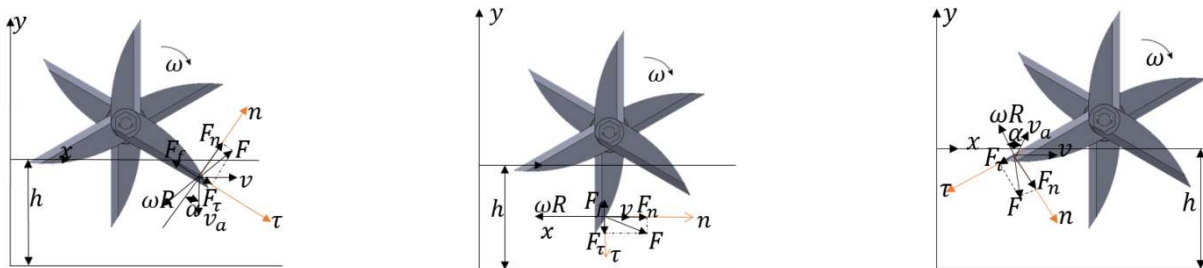


FIGURE 4. Forces on the shovel handle during operation.

friction, etc. Since there are no stones or other debris in the soil, the cutting effect is very small, and the cutting resistance can be neglected in the force analysis (Gill et al., 1983); thus, the operating resistance is $F = F_0 + F_3$ to the soil lifting device. Therefore, the entry angle of the lifting device α is adjusted to reduce the resistance, but the angle is too large or too small to affect the soil lifting effect, and thus the entry angle of the lifting device is between 40° and 50° . From [eq. (2)], the lift angle β has a significant effect on the resistance to the lift, mainly affecting the forward resistance of the lift, which increases as the angle increases. With decreasing angle, the resistance is reduced, but the lifting soil effect is poor. Combined with the agricultural machinery design, the manual lifting angle of the soil lifting device is in the range of $18^\circ \sim 20^\circ$.

Force analysis of the soil crushing knife

In this design, the front lifting device lifts the soil, and then the soil comes in contact with crushing knife to crush the soil as shown in Figure 5.



(a) When a blade tooth enters the soil (b) When a blade tooth is deepest in the soil (c) When a blade tooth leaves the soil

FIGURE 5. Force analysis of the operation of the soil crushing knife.

Where:

F_f is the frictional resistance of the soil breaking blade during operation and h is the maximum depth of soil penetration of the soil breaking blade;

v is the forward speed of the soil breaking blade during operation;

ω is the angular speed of rotation of the soil breaking blade;

R is the radius of the rotation of the soil breaking blade;

the combined speed v_a of v and ωR and the angle α normal to the edge of the soil breaking blade define the slip tangent angle;

F is the reaction force of the soil on the soil crushing blade when the soil crushing blade is plowed, and

the force is decomposed on the n -axis and τ -axis to obtain the normal force F_n and the tangential force F_t on the soil crushing blade as:

$$F_t = F \sin \alpha \quad (3)$$

$$F_n = F \cos \alpha \quad (4)$$

The above equation leads to the calculation of F_f as:

$$F_f = \mu F_n \quad (5)$$

$$\mu = \tan \varphi \quad (6)$$

in which:

μ - the friction factor between the soil crushing knife and the soil;

φ - the soil friction angle.

To reduce the resistance during the operation of the soil breaking blade, the force in the direction perpendicular to the knife edge should be reduced, and the force in the direction tangential to the knife edge should be increased to satisfy the following:

$$\begin{cases} F_f < F_t \\ \mu F_n < F \sin \alpha \\ \tan \varphi F \cos \alpha < F \sin \alpha \\ \alpha > \varphi \end{cases} \quad (7)$$

When the soil crushing knife cuts the soil, the soil is considered a mass, and the force analysis of the soil is shown in Figure 6.

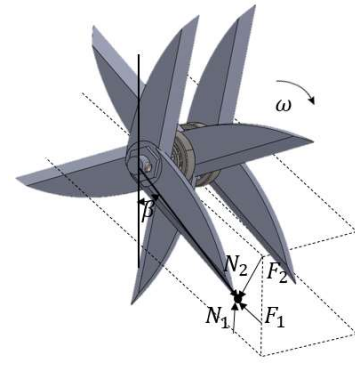


FIGURE 6. Soil force analysis.

In Figure 6, N_1 is the supporting force between the soil; N_2 is the normal force on the soil in the operating state of the soil crushing knife; β is the angle between the line of action and the center of rotation and the vertical direction; F_2 is the tangential force of the soil crushing knife on the soil; and F_1 is the frictional force of the soil on the soil crushing knife.

To ensure that the clods are cut off, it is necessary to satisfy the following relationships in the vertical and horizontal directions:

$$N_1 = N_2 \cos \beta + F_2 \sin \beta \quad (8)$$

$$F_1 + F_2 \cos \beta > N_2 \sin \beta \quad (9)$$

$$F_1 = N_1 \tan \varphi_1 \quad (10)$$

$$F_2 = N_2 \tan \varphi_2 \quad (11)$$

in which:

φ_1 - the friction angle between soils,

φ_2 - the friction angle between soil cutter and soil.

Substituting Formulas (10) and (11) into Formula (9) yields:

$$N_1 \tan \varphi_1 + N_2 \tan \varphi_2 \cos \beta > N_2 \sin \beta \quad (12)$$

Substituting Formula (8) into Formula (12) yields:

$$N_2 \cos \beta \tan \varphi_1 + N_2 \tan \varphi_2 \sin \beta \tan \varphi_1 + N_2 \tan \varphi_2 \cos \beta > N_2 \sin \beta \quad (13)$$

Therefore,

$$\beta < \varphi_1 + \varphi_2 \quad (14)$$

β satisfies:

$$\cos \beta = \frac{R - h}{R} \quad (15)$$

Substituting Formula (15) into Formula (14) yields:

$$\cos^{-1} \frac{R - h}{h} < \varphi_1 + \varphi_2 \tag{16}$$

Therefore, if the cutting resistance is reduced, then the sliding cutting effect should be increased, resulting in the relative acceleration determined by the edge curve. The fitting curve in the reference from the literature applies it to the rear edge of the soil breaking tool designed in this project. All coordinate points are obtained by fitting the curve equation, and the fitting curve diagram is derived by MATLAB (Zhao et al., 2019), as shown in Figure 7. Under the condition of minimizing the force on the soil breaking knife, it is necessary to meet the requirement that the sliding cutting angle of the soil breaking knife edge design is larger than the friction angle of its contact with the soil. According to the literature, the cutting angle is generally 30~50° (Zhao et al., 2019), and thus the cutting angle is taken as a factor for experimental verification. To ensure better completion of the soil lifting operation and reduce the working resistance, this design selects the depth of the soil lifting knife to be 220~300 mm because the larger the radius R of the soil lifting knife is, the smaller the friction angle. Considering the depth limit of the soil lifting device, the radius of the soil breaking knife in this design is 250 mm.

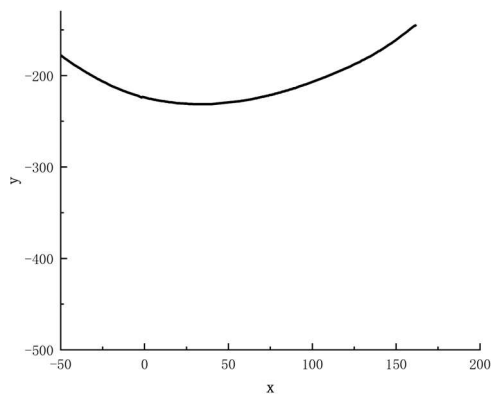


FIGURE 7. Fitting curve of the soil cutter.

EDEM simulation

EDEM particle parameter calibration

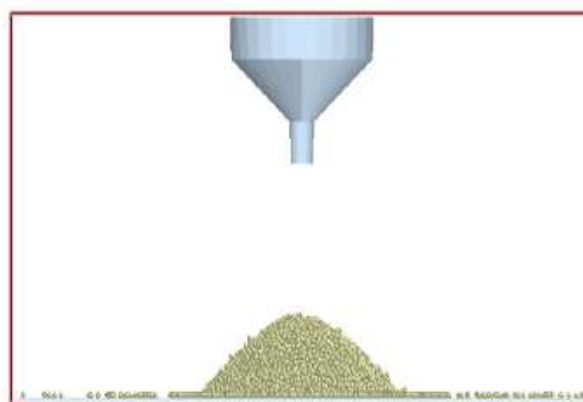
In this study, soil samples were selected from the test soil trough (36.81° N, 117.99° E) of Shandong University of Technology in Zibo City. Due to the complex characteristics of soil, such as discontinuity, nonlinearity and heterogeneity, it is difficult to understand the characteristics of the soil from the perspective of continuum mechanics (Li et al., 2019). The discrete element method has unique advantages in describing the properties of granular materials and has been widely used in the study of soil mechanical properties. However, the true behavior of the soil medium largely depends on the choice of contact model and the determination of mesoscopic parameters. Therefore, it is of great importance to quickly and accurately determine the mesoscopic parameters of the soil discrete element model for the study of soil properties.

Angle of repose of soil

The static friction coefficient and the rolling friction coefficient between soil particles are calibrated by the angle of repose test (Zang et al., 2017), which is mainly used to evaluate the fluidity of soil and the friction between particles. In this study, the funnel method was used to measure the angle of repose of soil, and the soil was slowly poured into the funnel (Ucugul et al., 2017; Ma et al., 2020). As the soil particles fall, the angle of repose of the soil pile is gradually formed, as shown in Figure 8 (a). The test was conducted three times, and the average value of the angle of repose of the soil pile was 32°. In the simulation, the soil particle simulation model was first established. The three-dimensional model of the test rig was constructed using SolidWorks software, and its dimensions were the same as the size of the hopper in the physical test. The simulation is shown in Figure 8 (b). The EDEM simulation was run twice, and the test results under the static and dynamic friction coefficients of 0.36~0.41 and 0.17~0.21, respectively, agreed well with the EDEM results.



(a) Angle of repose test equipment



(b) Simulation of the angle of repose test

FIGURE 8. Angle of repose test.

To reduce the measurement error caused by human factors, MATLAB was used to process the collected images (Wang et al., 2016). After reading the test image into MATLAB, the image as processed in grayscale and binarized, as shown in Figure 9.

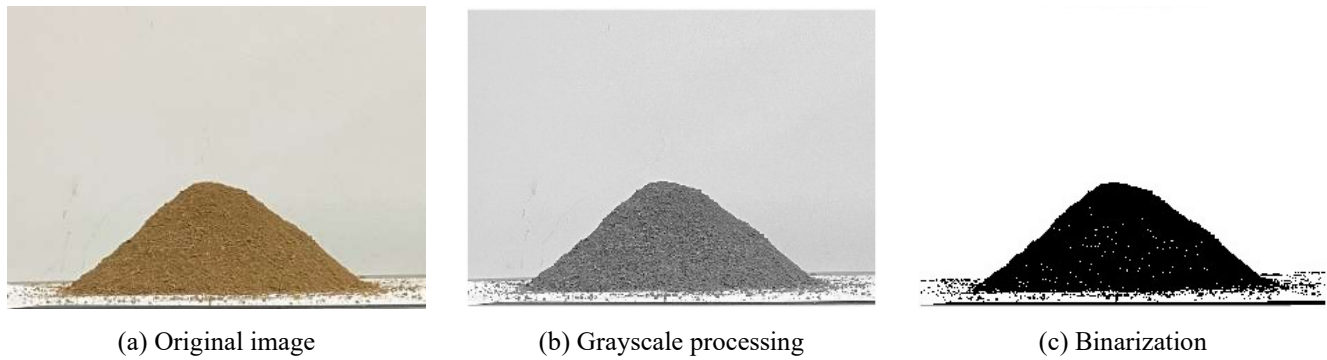


FIGURE 9. Image processing of the angle of repose.

Finally, the boundary points were extracted. The line on the boundary was the boundary curve of the soil. The least square method was used to fit the boundary points. As shown in Figure 10, the slope of the fitted line was the tangent of the measured angle of repose.

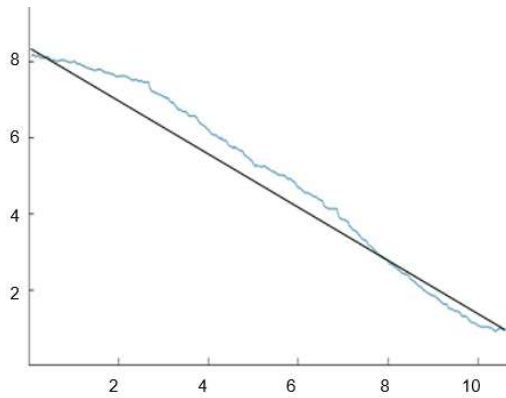


FIGURE 10. Linear fit of the image of the angle of repose.

Angle of soil sliding friction

The slope test of soil particles was conducted according to the material sliding friction angle test bench that was fabricated in this laboratory (Dai et al., 2019). Before the test, the test bench was placed horizontally, the soil s placed on the steel plate, and the test bench was slowly raised at a constant speed of 2°/s so that the included angle between the test bench and the horizontal plane gradually increased. When the soil slid with the inclined plane, the adjustment was stopped, and the included angle between the test bench and the horizontal plane was recorded as the soil sliding friction angle (Zhao et al., 2021). To accurately measure the soil sliding friction angle and ensure that the attitude and posture of the soil were consistent each time, each group of measurements was repeated three times, and the test results

were averaged. The results of the measurements are shown in Table 1. In the simulation test, 0.8 kg of particles was generated. After the particles were generated, the inclined plane was rotated around the fixed axis of the inclined plane at a rotational speed of 2°/s until the generated particles slid on the inclined plane, and the simulation ended. The static friction coefficient and dynamic friction coefficient of soil were - 65 Mn are 0.36 and 0.17, respectively, according to the final calculation.

TABLE 1. Soil-65Mn sliding friction angle.

Parameter	Soil		
	1st time	2nd time	3rd time
Scope	31.0~37.0	23.0~39.0	33.0~41.0
Average value	33.0	30.3	37.0

Soil shear test

The shear strength of the soil was measured by the direct shear test using a constant strain direct shear apparatus (ZJ-type direct shear apparatus), as shown in Figure 11. During the test, the upper part was sheared by applying different vertical pressures of 50, 100, 150 and 200 kPa through the rigid loading device, and the strain rate was 2.4 mm/min. The theoretical formula for the soil shear test was the Coulomb formula (Jiang et al., 2017).

$$\tau = c + p \tan \varphi \tag{16}$$

in which:

τ - shear stress;

c - soil cohesion;

p -vertical pressure,

φ - internal friction angle of soil.

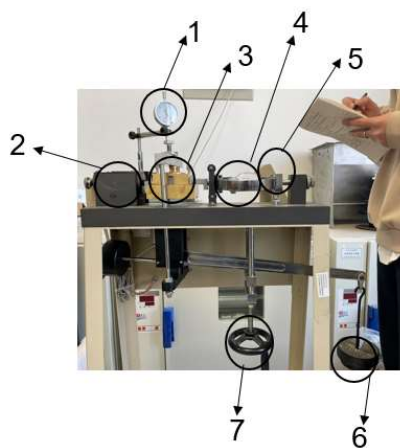


FIGURE 11. Soil shear test.

1. Dial gauge, 2. Propulsion motor, 3. Shear box, 4. Force measuring ring, 5. Controller, 6. Hanging plate, and 7. Leveling handwheel

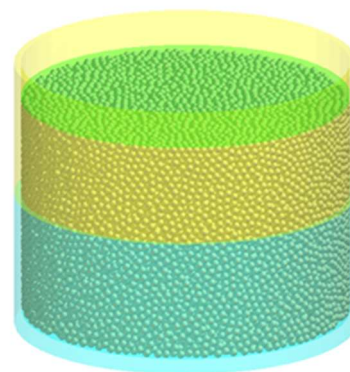


FIGURE 12. Shear simulation test.

The angle of internal friction of the soil was calculated from the slope k of the strength line, i.e., $\varphi = \arctan k$. The shear stress was $\tau = C_0 R$ where C_0 was the force ring calibration coefficient equal to 1.587 KPa/0.01 mm (Liu et al., 2022), and R was the maximum reading of the force ring micrometer. The shear strength curve was drawn according to the corresponding shear stress and normal compressive stress, and the results for the shear stress under four loads are shown in Table 2.

TABLE 2. Shear stress under different loads (KPa).

Parameter	Vertical pressure/KPa			
	50	100	150	200
Average value	94.38	112.76	136.68	158.16

The internal friction angle of the test soil was 21.93° , and Poisson's ratio [24] calculated from the internal friction angle was 0.38. Following the principle of the shear test, the simulation model was set up as shown in Figure 12. The size of the shear box was 20 mm high and 61.8 mm in diameter. The upper and lower shear boxes were open, the upper part of the lower shear box was open, and the lower part was closed (Song et al., 2022). The vertical load on the soil model was added by setting the vertical downward velocity on the pressure plate of the upper shear box, and the contact force between the soil particles and the pressure plate in the vertical direction was the vertical load of the shear test simulation (Ucguil et al., 2015; Wang et al., 2017). During the simulation, the lower shear box sheared the soil at a horizontal speed of 2.4 mm/min. The post-processing function of the EDEM software was used to derive the force on the simulation model. The shear strength curve was drawn from the data in Table 2, as shown in Figure 13.

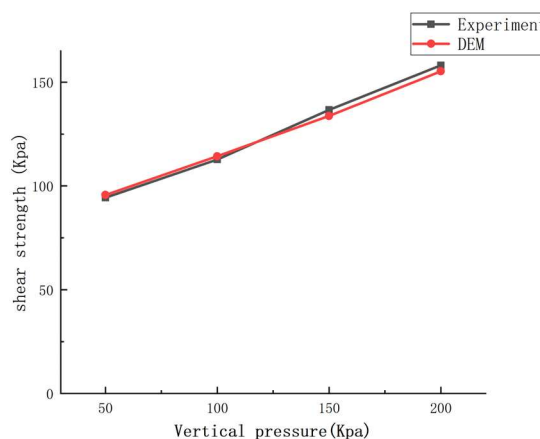


FIGURE 13. Shear strength curve.

Establishment of the discrete element simulation model

Soil particles

To simulate soil from the field, it was very important to create simulated soil particles. According to the characteristics of the test soil, the Hertz–Mindlin with bonding model in EDEM was selected to simulate the binding forces between soil particles, which was represented by bonds (Ding et al., 2017), as shown in Figure 14. The shape of the soil particle unit under the Hertz–Mindlin with bonding model is relatively small for the interaction between soil particles, which can more accurately simulate the interaction process between tillage components and soil (Zhao et al., 2017). Therefore, the basic spherical particles in EDEM were chosen as the soil particle unit in this study. If the particle parameter size is too small for discrete element simulation, then it affects the simulation time. Thus, based on the literature about setting the radius of soil particles for discrete element simulation, in this study the soil particles were set to a single particle of 6 mm (Zhao et al., 2021).

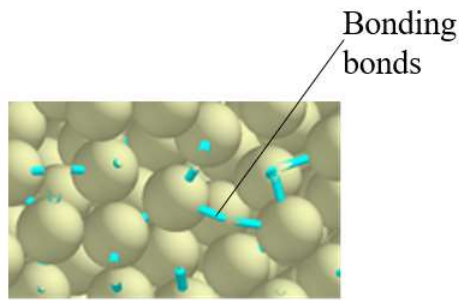


FIGURE 14. Inter-particle bond.

EDEM simulation model

The soil tank size was 1200 mm×600 mm×400 mm, particles were generated, and the tank was filled with particles based on gravity. The total number of particles was 192,448, and the number of bonds was 769,224, according to Table 3.

Option 4 in the EDEM pre-processor module was used to establish the contact mechanics model, soil particle model, and geometric model settings; the soil tank was filled with particles for settling so that the particles could establish good bonds. In the EDEM software, the model parameters included material parameters and contact parameters, and the material parameters included Poisson's ratio, density, and shear modulus of the working tool and soil, where the main material of the working tool was 65Mn, the speed was set to 1.5 m/s (Cao et al., 2021), and the depth of the soil was 220 mm, where the density and shear modulus parameters of 65Mn are shown in Table 4 (Zhao et al., 2017). The geometric model of the wheel rut tillage device was created using SolidWorks 2020, the device was saved in step format, and the geometric simulation model was saved in IGS format and imported into EDEM. Finally, the particle displacement and resistance of the device were exported using the file option of the EDEM post-processing interface.

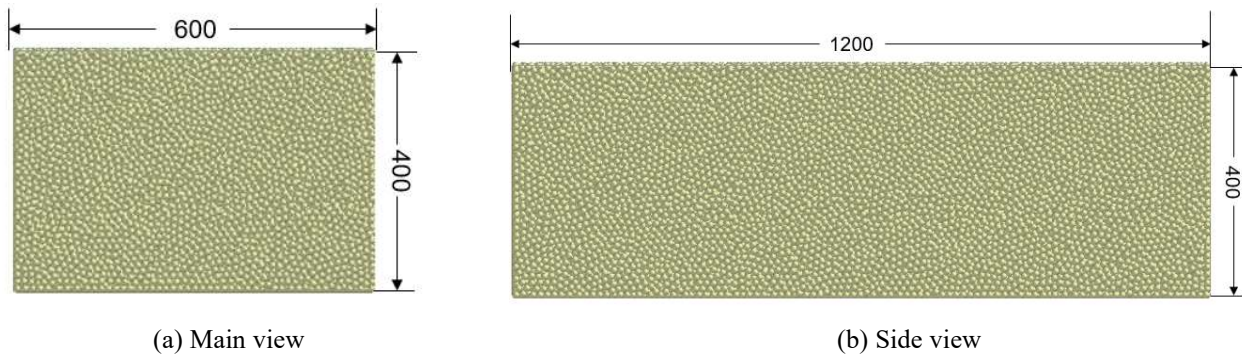


FIGURE 15. Soil trough model.

TABLE 3. Soil model simulation parameters.

PARAMETERS	VALUE
Poisson's ratio	0.38
Shear modulus <i>Pa</i>	1.24×10^6
Density <i>Kg · m⁻³</i>	2150
Recovery factor	0.6
Static friction coefficient	0.36
Coefficient of dynamic friction	0.17
Normal stiffness <i>N/m</i>	3.4×10^8
Tangential stiffness <i>N/m</i>	1.5×10^8
Normal critical stress <i>Pa</i>	2×10^5
Tangential critical pressure <i>Pa</i>	6.8×10^4

TABLE 4. Simulation parameters of the integrated lifting and shredding device.

PARAMETERS	VALUE
Poisson's ratio	0.3
Shear modulus <i>Pa</i>	7.27×10^{10}
Density <i>Kg · m⁻³</i>	7865
Recovery factor	0.6
Static friction coefficient between particles and deep loosening shovel	0.6
Coefficient of dynamic friction between the particles and the deep loosening shovel	0.05

Simulation Analysis and Results

Particle motion

To investigate the movement of the soil under the operation of the wheel rut tillage device, soil particles were selected in the direction of advance of the wheel rut tillage device and the middle particle as a reference to disperse the two sides, and soil particles that met the conditions of the tillage depth range of seven markers were used as tracers. The simulation model at this time was more stable, and the data were more accurate compared to the state when the soil lifting device first entered and left the soil, and the selected soil particle distribution is shown in Figure 16. Six soil particles at each of the seven locations were selected vertically downward, and their vertical movement was tracked.

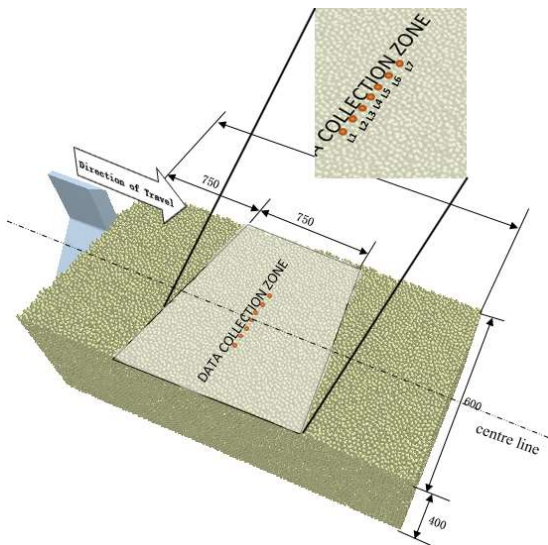


FIGURE 16. Soil particle distribution map.

In the simulation of the soil lifting device, when the soil lifting device started to enter the soil, the soil particles started to move upward under the effect of the inclination angle of the soil lifting device. After the soil lifting device entered the soil and drove the surrounding soil to move, the soil in front was squeezed to complete the lifting operation because of the mutual effect between the soils. The green arrow represents the trend of the vector of particle displacement at the edge of the operation because the distance from the lifting device was too far upward and was not as obvious compared with the middle zone. However, the overall trend was still upwards, and the velocity vector diagram shows that the lifting device could lift the soil well.

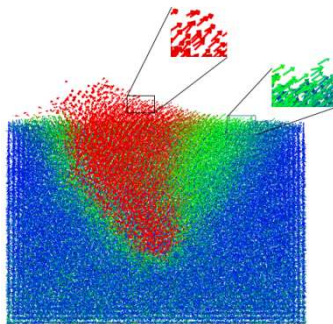


FIGURE 17 Soil particle vector distribution.

The displacement curve of the vertical movement of the marked soil particles was obtained by the lifting process of the soil lifting device, as shown in Figure 18. When the soil particles were first inserted into the soil by the lifting device during the simulation, the marker tracer showed a small lifting behavior due to the force between the soil and the soil and then fell back to a position higher than the original position. As the working surface of the lifting device gradually approached the calibration particles, the soil particles were lifted and picked up by the action of the shovel tip, and the soil particles began to move upwards. As the lifting device passed through the soil particles, the lifted soil particles began to fall back under their own gravity and become stable.

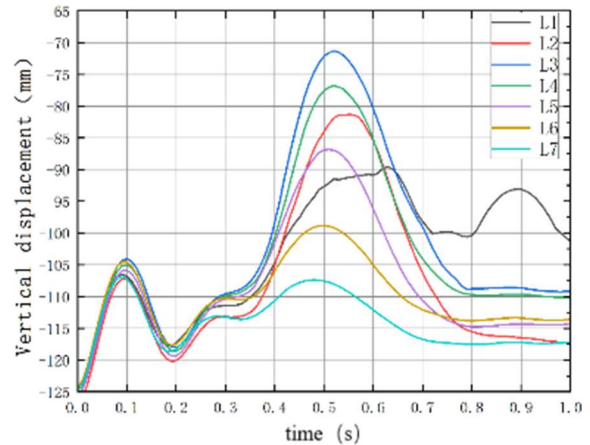


FIGURE 18. Movement of soil particles at different locations during the operation

According to the simulation analysis, the lifting device started to pass the marked soil particles at approximately 0.3 s. As the lifting device moved, the marked soil particles were slowly lifted under the action of the lifting device at 0.52 s, and the marked soil particles were lifted to the maximum height. Since the marked soil particles were located in the center of the soil model, the lifting performance of the lifting device was further verified by calculating that the lifting device had completely passed the marked soil particles by multiplying the time by the displacement speed of the device. At this point, the marked soil particles started to fall back and become stable for a period of time thereafter.

The lifting performance of the lifting device at different entry angles, lifting angles and offset distances is shown in Figure 19. With the passage of time, the displacement of soil particles in the vertical direction gradually increased to a peak and then gradually decreased. Figure 19(a) shows that the lifting device lifted soil particles to the greatest height at an angle of 40°, followed by 45°, and finally 50°. Figure 19(b) shows that as the lifting angle of the device decreased, the device became less effective in lifting soil. The effect of the device offset distance on the lift is shown in Figure 19(c); as the offset distance increased, the lifting effect became more pronounced. Analysis of the data showed that the implement displaced the most soil and had the best lifting effect at an entry angle of 40°, a lift angle of 28° and an offset distance of 175 mm.

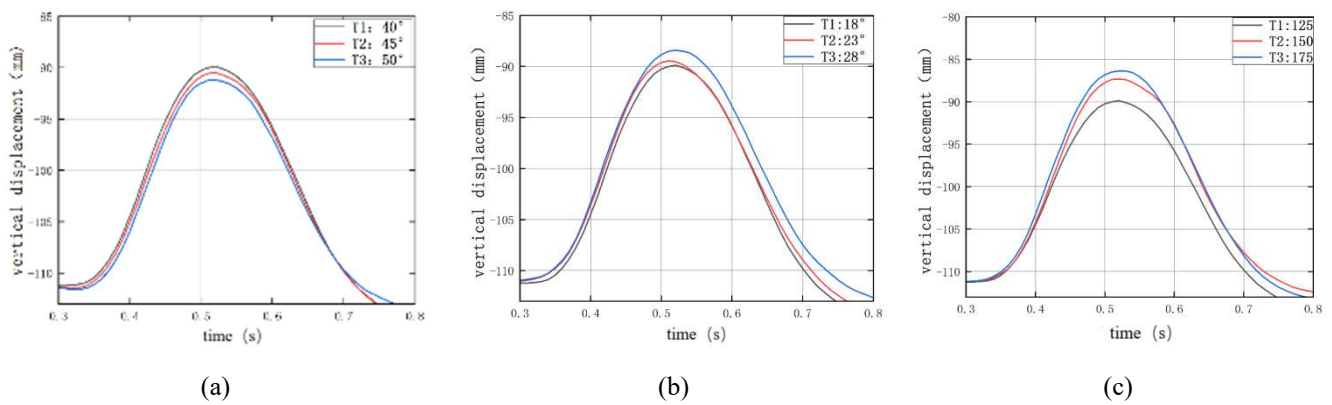


FIGURE 19. Variation of soil particle displacement for different factors during tillage (a) effect of entry angle, (b) effect of lifting angle, and (c) effect of offset distance.

Machine resistance

The amount of resistance of the machine is related to its energy consumption and is an important indicator used to evaluate the performance of the machine. Using the pulling resistance of the implement as the vertical coordinate and the time as the horizontal coordinate, the traction pulling of the implement was plotted against the ground angle, lift angle and offset distance, as shown in Figure 20.

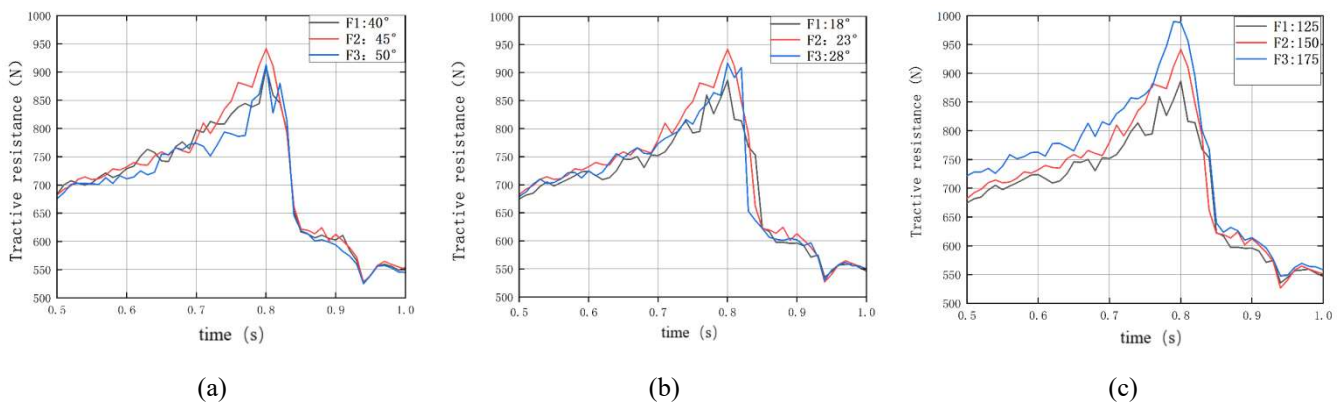


FIGURE 20. Traction resistance of the device during tillage (a) Resistance of the device at different angles of entry, (b) Resistance of the device at different lifting angles, and (c) Resistance of the device at different offset distances.

The results of all the outputs were averaged to give an average traction resistance of 633.98 N, 637.22 N, and 627.83 N for the 40°, 45°, and 50° device angles of entry, respectively. The average traction resistances of the device were 628.86 N, 637.56 N and 632.85 N for the 18°, 23° and 28° lift angles, respectively, and 628.86 N, 637.22 N and 696.32 N for the 125 mm, 150 mm and 175 mm offset distances, respectively. The traction resistance and energy consumption were lowest at the 18° lift angle and 125 mm offset distance.

Tests of soil lifting devices

Evaluation indicators

The soil lifting device is one of the most important working parts of the wheel rut cultivator for lifting compacted soil. The performance of a wheel rut tiller device depends mainly on the height of the soil particle lift and the resistance to the implement itself. Therefore, in this test, the soil particle displacement X and the resistance F applied to the implement were selected as the operating performance evaluation indices. The maximum soil particle displacement was the maximum

displacement height of the calibration particles. After the soil lifting operation, the maximum average displacement of the calibration particles was selected and measured five times. The resistance to the device was the resistance to the device in the forward direction after the lifting device passed through the soil and was expelled at the EDEM post-processing interface.

Secondary orthogonal combination test design

To further investigate the effect of the structural parameters of this pair of wheel rut tillage implements on the lifting height of soil particles and the resistance to the implement, a combined quadratic orthogonal regression test was performed using EDEM simulation software. Three key parameters (X1, X2, X3) affecting the soil lifting effect were selected as factors. The particle lifting height and the resistance to the device were selected as test indices, and a 3-factor, 3-level quadratic orthogonal regression test was designed using Design-Expert10 software to investigate the relationship between the key factors and the test indices. The orthogonal test factors and levels are shown in Table 5.

TABLE 5. Factors and levels of the quadratic orthogonal regression combination test for the operational effect of the soil lifting device.

Factor level	Angle of entry	Lifting angle	Offset distance
-1	40	18	125
0	45	23	150
1	50	28	175

Simulation test results and analysis

The test results are shown in Table 6, where X1, X2 and X3 are the coding values of the device offset distance, soil entry angle and lifting angle, respectively.

TABLE 6. Quadratic orthogonal regression combination test scheme and results of operation effect of soil lifting device.

Test serial number	Factor			Soil particle displacement/ Y_1	Resistance/ Y_2
	Offset distance/ X_1	Angle of penetration/ X_2	Lifting angle/ X_3		
1	125	45	18	49.02	628.86
2	125	50	23	49.63	627.83
3	175	45	18	49.55	637.69
4	150	40	28	56.41	642.27
5	175	50	23	48.84	637.19
6	175	40	23	50.69	644.94
7	125	45	28	57.41	632.85
8	150	50	28	50.86	634.16
9	150	45	23	53.12	637.22
10	175	45	28	53.01	642.76
11	125	40	23	53.98	633.98
12	150	50	18	50.98	628.72
13	150	45	23	52.01	637.22
14	150	40	18	51.86	638.08
15	150	45	23	51.98	638.34
16	150	45	23	52.98	635.21
17	150	45	23	51.32	636.37

Regression equation

The experimental data were analyzed using Design-Expert10 software, and the F test was performed at a confidence level of $\alpha=0.05$. The partial sums of squares and

degrees of freedom of insignificant factors and interactions were combined into the remaining sum of squares and then re-analyzed to ensure that there were suitable factors, or significant levels, to obtain optimized equations:

$$Y_1 = 52.28 - 0.9937x_1 - 1.58x_2 + 2.03x_3 + 0.625x_1x_2 - 1.23x_1x_3 - 1.17x_2x_3 - 0.8885x_1^2 - 0.6085x_2^2 + 0.854x_3^2$$

$$Y_2 = 636.87 + 4.88x_1 - 3.92x_2 + 2.34x_3 - 0.4x_1x_2 + 0.27x_1x_3 + 0.3125x_2x_3 - 0.5772x_1^2 - 0.3097x_2^2 - 0.7548x_3^2$$

Regression equation variance analysis

As shown in Tables 7 and 8, the regression models for both indicators were highly significant ($P < 0.01$), indicating that the selected models were appropriate and that there was a model-determined relationship between the test indicators and the test factors. None of the misfit terms were significant ($P > 0.1$), indicating that the model was appropriate and that

no uncontrolled factors had an effect on the indicators, while the model fit was good. The regression model in Table 7 shows that the weights of the effects on the lifting height of soil particles were in the following order: implement lifting angle, soil entry angle, and offset distance. The regression model in Table 8 shows that the weights of the effects on the implement resistance were in the following order: implement offset distance, soil entry angle and lift angle.

TABLE 7. Results of the ANOVA analysis of the regression analysis of the simulation of lift heights of soil particles.

Projects	Sum of squares	Degree of freedom	Mean Square	F	P
Models	81.71	9	9.08	6.93	0.0092
X_1	7.90	1	7.90	6.03	0.0438
X_2	19.94	1	19.94	15.21	0.0059
X_3	33.13	1	33.13	25.28	0.0015
X_1X_2	1.56	1	1.56	1.19	0.3110
X_1X_3	6.08	1	6.08	4.64	0.0683
X_2X_3	5.45	1	5.45	4.16	0.0808
X_1^2	3.32	1	3.32	2.54	0.1553
X_2^2	1.56	1	1.56	1.19	0.3115
X_3^2	3.07	1	3.07	2.34	0.1697
Residuals	9.17	7	1.31		
Misfit value	6.89	3	2.30	4.03	0.1057
Error	2.28	4	0.5700		
Total	90.89	16			

TABLE 8. Analysis of variance of the regression of the simulation of the resistance to the device.

Project	Square	Degrees of freedom	Mean square	F	P
models	363.34	9	40.37	38.41	<0.0001
X_1	190.71	1	190.71	181.45	<0.0001
X_2	123.01	1	123.01	117.04	<0.0001
X_3	43.66	1	43.66	41.54	0.0004
X_1X_2	0.64	1	0.64	0.6089	0.4608
X_1X_3	0.2916	1	0.2916	0.2774	0.6147
X_2X_3	0.3906	1	0.3906	0.3717	0.5614
X_1^2	1.40	1	1.40	1.33	0.2858
X_2^2	0.404	1	0.404	0.3844	0.5549
X_3^2	2.40	1	2.40	2.28	0.1746
Residuals	7.36	7	1.05		
Misfit value	1.95	3	0.6486	0.4794	0.7139
Error	5.41	4	1.35		
Total	370.69	16			

Optimization of structural parameters

The optimal combination of parameters was obtained using the optimal combination module in Design-Expert10 with the highest possible lifting height of the soil particles and the lowest possible resistance to the device as the target as follows: the offset distance of the device was 125 mm; the entry angle was 43.6°; the lift angle was 28°; the lifting height of the soil particles at this time was 57.41 mm; and the pulling resistance of the device was 633.603 N.

Simulation test of the optimized soil lifting device with a soil crushing device

Based on the parameters of the soil lifting device and the soil crushing blade obtained from the above analysis, SolidWorks was used to build a 3D model of the part and to assemble and check the interference of the soil crushing blade.

The virtual prototype model of the ripper was imported into RecurDyn after assembly, and RecurDyn was used to add mass properties to the ripper, rotate and move subsets to the crusher blade and add forward constraints to the moving subsets and other simulation parameters. EDEM-RecurDyn coupled crusher blade motion subsets were added as shown in Table 9.

TABLE 9. Addition of working device motion subsets.

Campaign sub	Binding
Mobile vice	Earth breaking knife
Rotating sub	Soil crusher-bearing
Mobile vice	Soil lifting device

The main purpose of the soil breaking blade in the soil breaking process is to break the bond between soil particles

to complete the final loosening operation. When the tiller cuts the soil, the bond of the soil discrete element model is broken due to shear stress. For in-depth study of the effects of the blade thickness and cutting edge angle of the soil crushing knife on the effect of soil crushing and to provide a basis for the design of the mechanism, full-factor tests were conducted. The blade thickness and cutting edge angle of the soil crushing knife were selected as factors and the number of broken soil bonds and the traction resistance to which the device was subjected were selected as indicators. The levels of each factor were selected separately according to the range of parameters, as shown in Table 10, and a total of nine trials were conducted.

TABLE 10. Single-factor test results.

Level	Knife thickness (mm)	Cutter cutting edge angle (°)
-1	4	30
0	5	40
1	6	50

Effect of cutting edge angle

The effect of different cutting edge angles on the number of bond fractures was simulated for three different tool thicknesses, as shown in Figure 21. The 30° cutting angle had the largest number of bond fractures with a fracture rate of 83.84% at a tool thickness of 4 mm. The 50° cutting angle had the largest number of bond fractures at a tool thickness of 5 mm with a fracture rate of 83.92%. At a knife thickness of 6 mm, the 40° cutting angle had the most bond fractures with a fracture rate of 83.99%. Figure 22(a) shows that the resistance was minimum at a cutting edge angle of 40°. Figure 22(b) shows that at only 0., the resistance was greater for the 40° cutting edge angle than the other angles, and at other times, the resistance of the 40° cutting edge angle is always less than that of the other two angles. Figure 22(c) shows that the resistance of the soil crushing knife was significantly less at the 40° cutting edge angle than the other angles. The above analysis showed that the number of bond breaks was greatest and the tensile resistance was smaller at the 40° cutting angle.

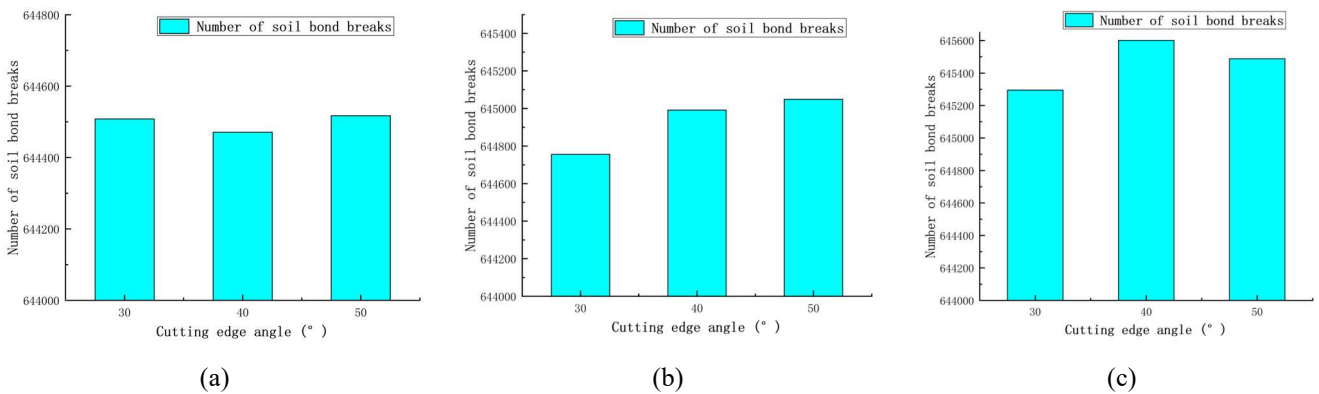


FIGURE 21. Effect of cutting edge angle on bond fracture at different insert thickness(a) 4 mm; (b) 5 mm; (c) 6 mm.

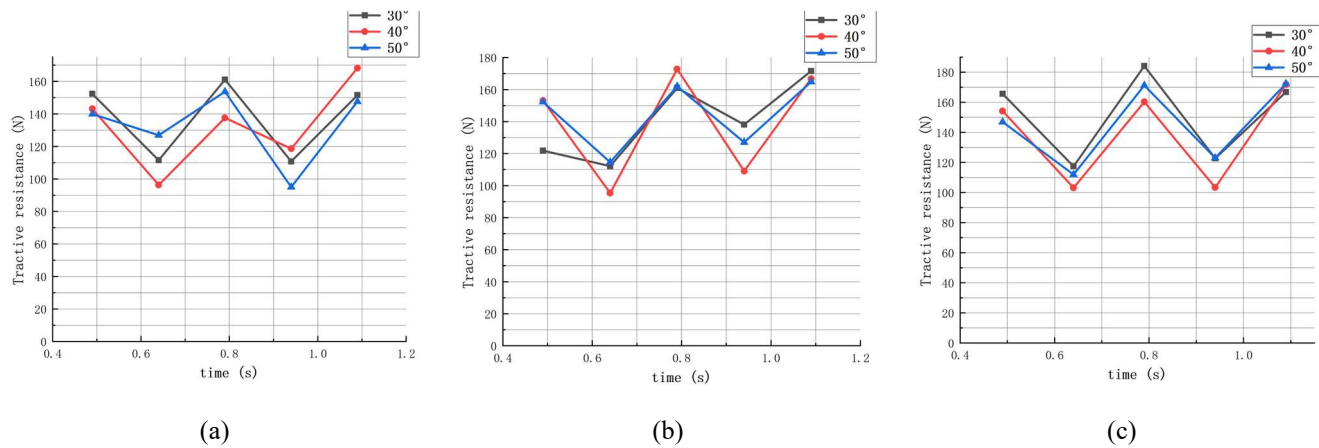


FIGURE 22. Effect of cutting edge angle on traction resistance for different insert thicknesses (a) 4 mm; (b) 5 mm; (c) 6 mm.

Influence of knife thickness

The simulated results of soil fracture for 4, 5 and 6 mm blade thicknesses were compared at a fixed working depth and speed, as shown in Figure 23. The number of bond fractures at each cutting angle increased with increasing tool thickness, the bond fracture rates were 83.95%, 83.99%, and 83.97%, and the difference in the effect of different tool

thickness dimensions on the number of bond fractures was approximately 0.02%. Figure 24(a) shows that the resistance was greatest for a tool thickness of 6 mm and least for a tool thickness of 4 mm. Figure 24(b) shows that the resistance was greatest when the tool thickness was 5 mm, and the resistance was least when the tool thickness was 4 mm. Figure 24(c) shows that the resistance was greatest at a tool thickness of 6 mm and least at 4 mm.

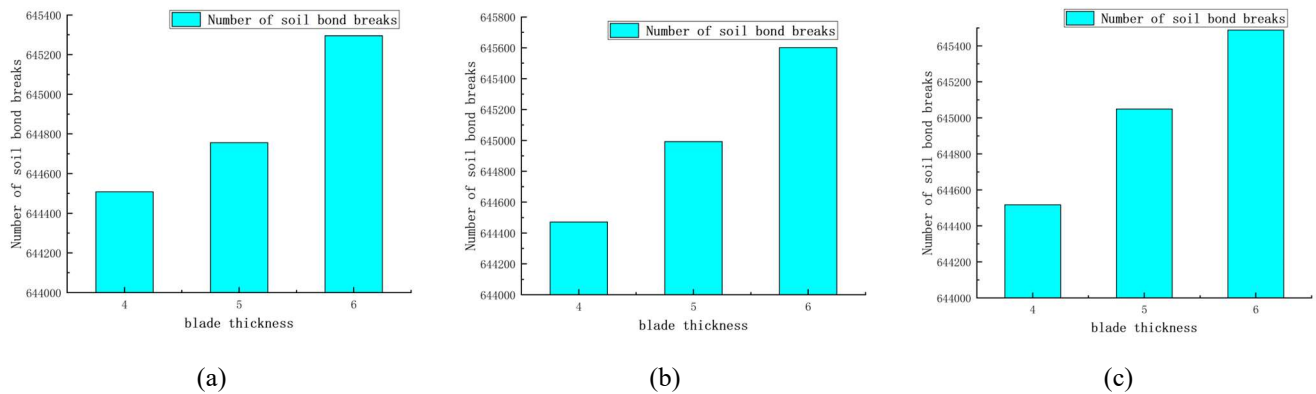


FIGURE 23. Effect of tool thickness on the number of bond fractures at different cutting edge angles (a) 30°; (b) 40°; (c) 50°.

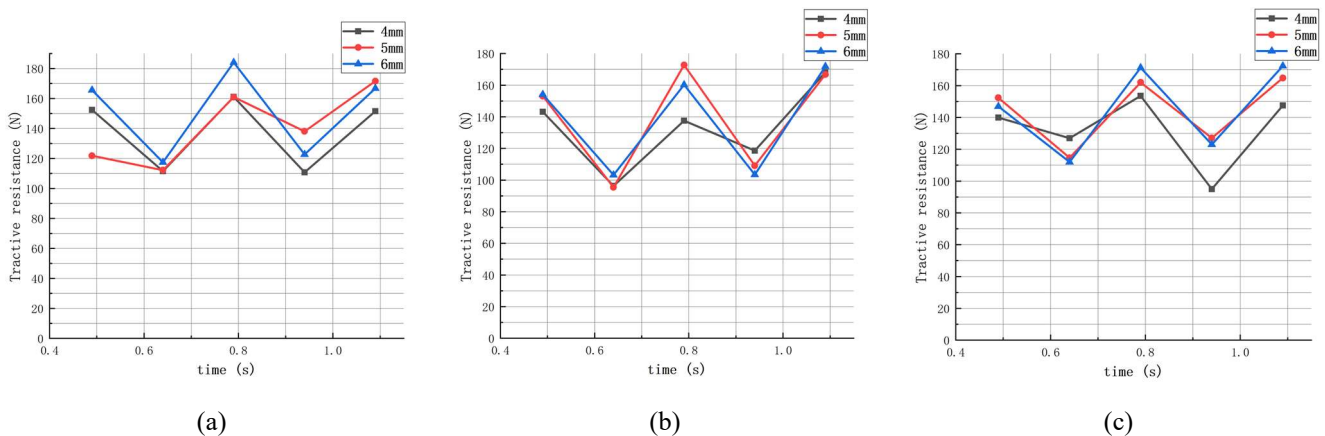


FIGURE 24 Effect of tool thickness on traction resistance at different cutting edge angles (a) 30°; (b) 40°; (c) 50°.

The above analysis is a summary of the data trends. To obtain the optimal parameters using Design-Expert10 for the test data from the full-factor test and analysis of variance, where A and B were the soil crushing device knife thickness and cutting edge angle, respectively, the analysis of variance of the test results is shown in Table 11.

TABLE 11. Analysis of variance.

	Projects	Sum of squares	Number of degrees of freedom	Mean square	F	P
Tractive resistance	Model	387.98	4	97.00	11.59	0.0179
	A	95.20	2	47.60	5.69	0.0677
	B	292.78	2	146.39	17.50	0.0105
	Residual	33.47	4	8.37		
	Cor total	421.45	8			
Number of broken bonds	Model	1.469E+07	4	3.673E+07	6.72	0.0460
	A	7.786E+07	2	3.893E+07	7.12	0.0481
	B	6.906E+07	2	3.453E+07	6.31	0.0579
	Residual	2.187E+07	4	5.468E+06		
	Cor total	1.688E+08	8			

From the ANOVA results in Table 4, it is clear that two factors, tool thickness and cutting edge angle, had significant effects on the traction resistance and number of broken bonds. By using the optimal combination module in Design-Expert10, the optimal combination of parameters was designed to minimize the resistance to the device and maximize the number of broken bonds as follows: The tool thickness was 6 mm, the cutting angle was 30°, the tensile resistance was 126.999 N, and the number of broken bonds was 648365.

Determination of parameters for the wheel rut soil crusher

The optimal parameters were obtained from the analysis of the orthogonal test of the soil lifting device and the full factor analysis test of the soil crushing knife, where the optimal parameters of the soil lifting device were as follows: the offset distance was 125 mm, the soil entry angle was 45° and the lifting angle was 28°. The thickness of the soil crushing knife was 6 mm, and the thickness of the cutting angle was 30°.

CONCLUSIONS

- (1) A real-time device for the reduction of compaction of soil in ruts was designed, the key parameters of the device were designed, and a model of the action of the soil lifting and crushing device was established. This device which effectively alleviates the problem of cumulative compaction of soil caused by the passing of tires.
- (2) A soil model applicable to loamy soils was established by applying the discrete element software EDEM. Comparing the virtual simulation with the real experiment showed that the soil model basically matched the soil properties of the test soil.
- (3) A quadratic regression of rotational data that combined orthogonal and single-factor simulation testing was used to obtain the primary and secondary factors affecting the performance of the soil lifting device by ANOVA: soil lifting device offset distance, soil entry angle and inclined lifting angle. The optimal combination was: device offset distance of 125 mm, soil entry angle of 43.592° and lifting angle of 28°. The full-factor test by EDEM-RecurDyn was used in a coupled simulation. The optimal parameters of the soil crushing device were a blade thickness of 6 mm and a cutting edge angle of 30°.

REFERENCES

- Berisso FE, Schjøning P, Keller T, Lamandé M, Etana A, Jonge LW de, Iversen BV, Arvidsson J, Forkman J (2012) Persistent effects of subsoil compaction on pore size distribution and gas transport in a loamy soil. *Soil and Tillage Research* 122 42-51. <http://dx.doi.org/10.1016/j.still.2012.02.005>
- Cao XP, Wang QJ, Li HW, He J, Lu CY, Yu CC (2021) Design and test of active rotary centralized straw cleaning device. *Journal of Agricultural Engineering* 37: 26-34
- Chen G, Weil RR (2011) Root growth and yield of maize as affected by soil compaction and cover crops. *Soil and Tillage Research* 117: 17-27. <http://dx.doi.org/10.1016/j.still.2011.08.001>
- Chen H, Yang YL (2012) Effect of tyre compaction on soil moisture infiltration properties. *Journal of Agricultural Mechanization Research*. 34: 153-156. <http://dx.doi.org/10.13427/j.cnki.njyi.2012.02.021>
- Dai F, Song XF, Zhao WY, Zhang FW, Ma HJ, Ma MY (2019) Simulated calibration of discrete element contact parameters for full film duopoly furrow mulch soils. *Transactions of the Chinese Society for Agricultural Machinery* 50(2): 49-56+77. <http://dx.doi.org/10.6041/j.issn.1000-1298.2019.02.006>
- Ding QS, Ren J, Adam BELAL Eisa, Zhao JK, Ge SY, Li Y (2017) Discrete element analysis of deep loosening process of wet clay paddy soil. *Transactions of the Chinese Society for Agricultural Machinery* 48(3): 38-48. <http://dx.doi.org/10.6041/j.issn.1000-1298.2017.03.005>
- Gao AM, Han ZS, Wu JF (2007) Experimental study of soil compaction in alfalfa fields by mowers. *Journal of Agricultural Engineering* 120: 101-105. <http://dx.doi.org/10.3321/j.issn:1002-6819.2007.09.018>
- Gao P, Sun JY, Gao JL, Yu XF, Wang ZG, Hu SP, Liu J, Bao HZ, Ji N (2020) Effect of deep loosening on soil physical structure and maize root system indicators in spring maize fields. *Northern Journal of Agriculture* 48: 103-108
- Gill WR, Vanden B, Glen E (1983) Tillage and traction soil dynamics.
- Hamza MA, Anderson WK (2005) Soil compaction in cropping systems. *Soil and Tillage Research* 82: 121-145. <http://dx.doi.org/10.1016/j.still.2004.08.009>
- Jiang Y, Li YJ, Xu Y (2017) Discrete element numerical simulation of direct shear test on sandy loam. *Journal Geotechnical Foundation* 31: 188-192. <http://dx.doi.org/CNKI:SUN:TGJC.0.2017-02-018>
- Keller T, Berli M, Ruiz S, Lamandé M, Arvidsson J, Schjøning P, Selvadurai APS (2014) Transmission of vertical soil stress under agricultural tyres: Comparing measurements with simulations. *Soil and Tillage Research* 140: 106-117. <http://dx.doi.org/10.1016/j.still.2014.03.001>
- Lamandé M, Schjøning P (2011) Transmission of vertical stress in a real soil profile. Part III: Effect of soil water content. *Soil and Tillage Research* 114: 78-85. <http://dx.doi.org/10.1016/j.still.2010.10.001>
- Li JW, Tong J, Hu B, Wang HB, Mao CY, Ma YH (2019) Calibration of discrete element simulation parameters for the interaction between clayey black soils of different water contents and contact soil components. *Journal of Agricultural Engineering* 35: 130-140

- Liu Y, Zhao J, Yin B, Ma Z, Hao J, Yang X, Feng X, Ma Y (2022) Discrete element modelling of the yam root–soil complex and its verification. *Biosystems Engineering* 220 55-72. <http://dx.doi.org/10.1016/j.biosystemseng.2022.05.002>
- Ma S, Xu LM, Yuan QC, Niu C, Zeng J, Chen C, Wang SS, Yuan XT (2020) Discrete element simulation parameter calibration for the interaction of grapevine chilling soil and soil clearing components. *Journal of Agricultural Engineering* 36: 40-49. <http://dx.doi.org/CNKI:SUN:NYGU.0.2020-01-005>
- Nawaz MF, Bourrié G, Trolard F (2012) Soil compaction impact and modelling. a review. *Agronomy for Sustainable Development* 33: 291-309. <http://dx.doi.org/10.1007/s13593-011-0071-8>
- Ren LD, Wang L, Lin L, Zhang B (2022) Research progress and prospect of agricultural soil mechanical compaction. *Journal of Soil Science*: 1-19.
- Schjønning P, Lamandé M, Berisso FE, Simojoki A, Alakukku L, Andreasen RR (2013) Gas diffusion, non-darcy air permeability, and computed tomography images of a clay subsoil affected by compaction. *Soil Science Society of America Journal* 77: 1977-1990. <http://dx.doi.org/10.2136/sssaj2013.06.0224>
- Song ZH, Li H, Yan YF, Tian FD, Li YD, Li FD (2022) Parameter calibration and experiment of discrete element simulation model for non-equal-diameter particles in mulberry garden soil. *Journal of Agricultural Machinery* 53: 21-33.
- Sun JB, Liu ZJ, Yang FZ, Sun Q, Liu Q, Luo PX (2023) A review of key technologies for agricultural equipment and slope operations in hilly and mountainous areas. *Journal of Agricultural Machinery*: 1-18
- Ucgul M, Fielke JM, Saunders C (2015) Three-dimensional discrete element modelling (DEM) of tillage: accounting for soil cohesion and adhesion. *Biosystems Engineering* 129: 298-306. <http://dx.doi.org/10.1016/j.biosystemseng.2014.11.006>
- Ucgul M, Saunders C, Fielke JM (2017) Discrete element modelling of top soil burial using a full scale mouldboard plough under field conditions. *Biosystems Engineering* 160: 140-153. <http://dx.doi.org/10.1016/j.biosystemseng.2017.06.008>
- Wang XL, Hu H, Wang QJ, Li HW, He J, Chen WZ (2017) Calibration method of soil model parameters based on discrete element method. *Journal of Agricultural Machinery* 48: 78-85. <http://dx.doi.org/10.6041/j.issn.1000-1298.2017.12.009>
- Wang YX, Liang ZJ, Zhang DX, Cui T, Shi S, Li KH, Yang L (2016) Discrete element-based calibration of interspecies contact parameters for maize seed particle models. *Journal of Agricultural Engineering* 32: 36-42. <http://dx.doi.org/10.11975/j.issn.1002-6819.2016.22.005>
- Zang Y, Han DL, Ji QL, He Y, Li JQ (2017) Study on the calibration method of sand and soil parameters in discrete element simulation. *Journal of Agricultural Machinery* 48: 49-56. <http://dx.doi.org/10.6041/j.issn.1000-1298.2017.03.006>
- Zhao SH, Liu HJ, Tan HW, Cao XZ, Zhang XM, Yang YQ (2017) Design and performance test of curvilinear trench opener on the head of pseudoflagfish. *Journal of Agricultural Engineering* 33: 32-39. <http://dx.doi.org/10.11975/j.issn.1002-6819.2017.05.005>
- Zhao SH, Liu HP, Yang C, Yang LL, Gao LL, Yang YQ (2021) Design and discrete element simulation of an interactive stratified deep loosening shovel for corn straw return. *Journal of Agricultural Machinery* 52: 75-87. <http://dx.doi.org/10.6041/j.issn.1000-1298.2021.03.008>
- Zhao SH, Wang JY, Yang C, Chen JQ, Yang YQ (2019) Design and testing of a stubble-breaking knife for conservation tillage. *Journal of Agricultural Machinery* 50: 57-68. <http://dx.doi.org/10.6041/j.issn.1000-1298.2019.09.007>